

Article

Parametric Analysis Using CFD to Study the Impact of Geometric and Numerical Modeling on the Performance of a Small Scale Horizontal Axis Wind Turbine

Muhammad Salman Siddiqui ^{1,*}, Muhammad Hamza Khalid ^{2,†}, Abdul Waheed Badar ^{3,†}, Muhammed Saeed ^{4,†}  and Taimoor Asim ^{5,†} 

¹ Faculty of Science and Technology, Norwegian University of Life Sciences, 1430 Ås, Norway

² Department of Electrical Engineering, Mathematics & Computer Science, University of Twente, 7500 AE Enschede, The Netherlands; m.h.khalid@utwente.nl

³ Department of Mechanical Engineering, HITEC University, Taxila 47050, Pakistan; abdul.waheed@hitecuni.edu.pk

⁴ Department of Mechanical Engineering, Khalifa University, Abu Dhabi 127788, United Arab Emirates; muhammed.saeed1@ku.ac.ae

⁵ School of Engineering, Robert Gordon University, Aberdeen AB10 7GJ, UK; t.asim@rgu.ac.uk

* Correspondence: muhammad.salman.siddiqui@nmbu.no; Tel.: +47-48-628035

† These authors contributed equally to this work.



Citation: Siddiqui, M.S.; Khalid, M.H.; Badar, A.W.; Saeed, M.; Asim, T. Parametric Analysis Using CFD to Study the Impact of Geometric and Numerical Modeling on the Performance of a Small Scale Horizontal Axis Wind Turbine. *Energies* **2022**, *15*, 505. <https://doi.org/10.3390/en15020505>

Academic Editor: Changkook Ryu

Received: 12 November 2021

Accepted: 14 December 2021

Published: 11 January 2022

Publisher's Note: MDPI stays neutral with regard to jurisdictional claims in published maps and institutional affiliations.



Copyright: © 2022 by the authors. Licensee MDPI, Basel, Switzerland. This article is an open access article distributed under the terms and conditions of the Creative Commons Attribution (CC BY) license (<https://creativecommons.org/licenses/by/4.0/>).

Abstract: The reliance on Computational Fluid Dynamics (CFD) simulations has drastically increased over time to evaluate the aerodynamic performance of small-scale wind turbines. With the rapid variability in customer demand, industrial requirements, economic constraints, and time limitations associated with the design and development of small-scale wind turbines, the trade-off between computational resources and the simulation's numerical accuracy may vary significantly. In the context of wind turbine design and analysis, high fidelity simulation under full geometric and numerical complexity is more accurate but pose significant demands from a computational standpoint. There is a need to understand and quantify performance deterioration of high fidelity simulations under reduced geometric or numerical approximation on a single small scale turbine model. In the present work, the flow past a small-scale Horizontal Axis Wind Turbine (HAWT) was simulated under various geometric and numerical configurations. The geometric complexity was varied based on stationary and rotating turbine conditions. In the stationary case, simple 2D airfoil, 2.5D blade, 3D blade sections are evaluated, while rotational effects are introduced for the configuration 3D blade, rotor only, and the full-scale wind turbine with and without the inclusion of a nacelle and tower. In terms of numerical complexity, the Single Reference Frame (SRF), Multiple Reference Frames (MRF), and the Sliding Meshing Interface (SMI) is analyzed over Tip Speed Ratios (TSR) of 3, 6, 10. The quantification of aerodynamic coefficients of the blade (C_l , C_d) and turbine (C_p , C_t) was conducted along with the discussion on wake patterns in comparison with experimental data.

Keywords: wind energy; horizontal axis wind turbine; computational fluid dynamics; high fidelity simulations; sliding mesh interface; multiple reference frame

1. Introduction

With the continuing surge in the world population, the global energy demand is set to increase in quite a considerate manner [1]. Environmental impacts of coal-based thermal power plants and long gestation periods associated with hydro plants render these technologies unfeasible for meeting future energy needs [2]. Wind energy presents itself as a feasible substitute owing to large availability, higher reliability, and fewer Green House Gas (GHG) emissions [3]. Wind turbines possess a considerable potential to increase the share of wind power in the overall energy mix. They are usually classified based upon their scale and configuration as a Horizontal-Axis Wind Turbine (HAWT) or a Vertical-Axis

Wind Turbine (VAWT), installed in large- or small-scale capacities [4,5]. The large-scale wind turbines are subject to the rough atmospheric effects and micro-scale turbulence effects [6–8]. However, in an urban rooftop setting, the wind flow structure is complex with larger skew angles, high turbulent content and large directional variability. Therefore, concerning zero-emission neighborhood, small-scale HAWT's have received increased attention in urban rooftop settings owing to their higher power output [9,10] compared to VAWTs and their ease of installation in an urban rooftop settings.

The significant interest in the deployment of small scale wind turbines calls for quick yet efficient methodologies to be employed in the preliminary design and analysis phase. Due to the higher costs affiliated with experimental setups, the reliance on numerical tools such as Computational Fluid Dynamics (CFD) has seen a rapid increase over the years [11]. Due to unsteady and disrupted wind conditions [12], and higher turbulent flows [13,14] in the urban neighborhood, CFD simulations becomes challenging and requires a careful selection of numerical models and appropriate geometries to obtain realistic estimations [15]. The computational cost becomes the main bottleneck concerning the choice of a particular modeling strategy.

In context of geometrical complexity, approximations based on simple two dimensional (2D) geometry are found to be computationally inexpensive. Nevertheless, such approximations offer significant implications on the accuracy of the final results. Studies by Devinant et al. [16] and Ferrari et al. [17], suggested the inadequacy of 2D simulations in accurately estimating the performance coefficients of wind turbines. Studies by Abraham et al. and Emeksiz et al. [18,19] showed that 2D simulations all-together lack providing details of flow disturbances caused by turbine structure (tower and nacelle) in particular for the downstream wake region. They suggested that such approximations are not deemed sufficient to draw general conclusions for a particular wind turbine model. Studies by [20–25] further comprehend the inadequacy of 2D simulations and conclude that three dimensional (3D) simulations are necessary to provide a clear assessment of flow physics around the wind turbine. Studies in [26,27] show that full-scale high fidelity simulations are viable choices to provide accurate estimations. However, the higher computational cost associated renders their selection unfeasible. The studies show that the optimal choice of the geometric approximation that maintains an optimal balance between computational costs and accuracy has been partially investigated previously. An in-depth investigation on a single turbine model is therefore imperative to comprehending such effects properly.

In the context of numerical complexity, methods such as Blade Element Momentum (BEM-CFD), Actuator Line model (ALM), Actuator Disk Model (ADM), Sliding Mesh Interface (SMI) and Multiple Reference Frame (MRF), etc. have been used for simulating flow past turbines. Rocchio et al. [28] suggested BEM-CFD based on ADM to predict the aerodynamic coefficients for wind turbines. They introduced the presence of blades through source terms in governing equations to predict the power coefficient of the turbine under given operating conditions. However, their method at low TSRs deviated significantly from the estimated solution. Guo et al. [29] performed a comparison of the BEM-CFD model against full rotor geometry simulations to analyze the flow physics of wind turbines. Their results showed that although the BEM-CFD coupled model is computationally inexpensive yet it overestimated the power coefficient against the full rotor model. They also showed that the BEM-CFD model reasonably predicted symmetrical features in wake profiles and circumferential velocity. However, in qualitative analysis, the full-scale rotor model performed better than the BEM-CFD model. The study by Siddiqui et al. [27] also showed that small flow features could only be accurately modeled using high fidelity CFD simulations. The comparison of ALM, SMI, and MRF by Tabib et al. [30] for an industrial-scale wind turbine showed differences for ALM and MRF in the region closer to the hub. At the same time, SMI captured the complex 3D captures accurately. Although SMI accurately predicts the flow features, it is found to be computationally expensive.

The computationally intensive nature of full-scale modeling and higher costs associated with simulations have led researchers to approximate flow problems by adopting simpler geometries. At one end, such modeling strategies have provided substantial speed-up. Still, at the same time, the extent of such approximations has been somewhat misunderstood due to the lack of wind tunnel measurements, which caused the drawing of implausible conclusions [26,31,32]. Tabib et al. [33] performed one such analysis of the flow patterns for megawatt turbines using full-scale 3D, 2.5D, and 2D approximations for a stationary blade. The 2D geometry showed unsatisfactory results close to the hub owing to three-dimensional complex flow structures, while a slightly better agreement was obtained away from the hub. However, in their CFD study, they only incorporated a stationary blade model while using additional source terms in the momentum equations to the model rotation. Their study lacked modeling of the physical geometrical rotation of turbine blades over the cycle. Siddiqui et al. [34] also investigated the modeling frameworks and geometric approximations utilizing rotating configurations for an industrial-scale turbine. High fidelity simulations are performed to capture the performance coefficient and wake profiles at various TSRs. However, the study lacks significant experimental evidence as there was no wind tunnel data to compare the solutions for the geometric and numerical approximations. A similar comparison on H-VAWT was performed by He et al. [35], who investigated the varying modeling complexity for 2D, 2.5D, 3D using Unsteady Reynolds-Averaged Navier Stokes (URANS) and Large Eddy Simulations (LES). However, the study is limited to a few test cases and does not investigate the influence of the tower and nacelle on wake deficits downstream. Santoni et al. [36] investigated the effect of the tower and nacelle on the velocity deficits in the wake region using CFD and suggested a strong influence on the velocity profiles in the wake deficits. A similar study by Abraham et al. [19] also suggested a strong influence of the tower on blade tip vortex breakdown and behavior of the near wake, owing to the strong interaction between the tower- and blade-generated flow structures. The aforementioned studies indicate a strong need to use full-scale high fidelity simulations; however, due to the restriction of computational resources and difficulty associated with full-scale modeling, it is imperative from the design standpoint to quantify the consolidated impact of numerical and geometric modeling on a single turbine model.

In the present study, an attempt is made to quantify a small-scale HAWT's aerodynamic performance compared to a full-scale modeling approach using stepwise increments in geometric and numerical complexity. This study aims to analyze the extent of geometric and numerical complexity to quantify the marginal trade-off between the accuracy and efficiency of numerical simulations using CFD. The Reynolds Average Navier Stokes (RANS) with the $k - \omega$ SST turbulence model is employed to simulate the aerodynamic coefficient and wake pattern under stationary and rotating conditions for a small-scale HAWT. The stationary case evaluates (i) simple 2D airfoil, (ii) 2.5D blade, and 3D blade sections. While in the rotating configuration, the simulations include geometries of (iii) 3D blade, (iv) rotor only, and (v) full-scale wind turbine inclusion the nacelle and tower. In terms of numerical complexity, a Single Reference Frame (SRF), Multiple Reference Frames (MRF), and a Sliding Meshing Interface (SMI) are analyzed over TSR of 6, 10. The performance parameters are quantified to calculate the extent of each approximation prediction against high fidelity full-scale modeling as well as the experimental results of Krogstad et al. [37,38]. To the best of the authors' knowledge, quantification of the consolidated influence of numerical and geometrical approximation on the performance of a single small-scale HAWT has not been conducted in the literature. Therefore, the present investigation provides a stepwise quantitative and qualitative analysis of wake evolution and turbine aerodynamic performance. It also highlights the extent of the prediction capability of each approximation in connection to computational complexity.

The distribution of the article is as follows. Section 2 gives a brief insight into the theoretical background and the definitions of performance parameters used for the study. Section 3 describes the details of the computational model and geometric approximations

considered in the present study. Section 4 highlights the important findings, along with a discussion of results. Section 5 reports the conclusion and future directions of work.

2. Theory and Background

2.1. Definition of Important Parameters

The Power coefficient C_p is defined as the fraction of actual power produced by the wind turbine to the total wind power available. Mathematically, C_p can be written as:

$$C_p = \frac{P_{out}}{\frac{1}{2}\rho AV_w^3}, \quad (1)$$

where P_{out} is power output from the wind turbine, A is the area, ρ is the air density, and V_w is the wind speed. From the design standpoint, the optimal choice of Tip Speed Ratio (TSR) is important for harnessing maximum power. TSR is defined as the ratio of the speed of the turbine blade at its tip with the actual wind speed. In the present study, we also investigate the effect of geometric and numerical approximations on the wake profiles and C_p at different tip speed ratios. Notable aerodynamic parameters that will be used for the study are dimensionless coefficients that are termed as the drag coefficient (C_d) and lift coefficient (C_l) and defined as follows,

$$C_D = \frac{F_D}{\frac{1}{2}\rho V^2 A}, \quad C_L = \frac{F_L}{\frac{1}{2}\rho V^2 A}. \quad (2)$$

where F_D and F_L are the drag and lift forces, respectively, and V is the flow velocity.

2.2. Governing Equations

2.2.1. Single Reference Frame (SRF)

SRF provides steady-state solutions when a single center of rotation is considered for a complete computational setup, and wall surfaces rotate at identical angular speeds. We adopt SRF under rotational periodic boundary conditions around the axis of rotation.

The governing equations in the present analysis have the following form:

$$\nabla \cdot \mathbf{u}_r = 0 \quad (3)$$

$$\frac{\partial \mathbf{u}_a}{\partial t} + \nabla \cdot (\mathbf{u}_r \otimes \mathbf{u}_r) + \underbrace{2\Omega \times \mathbf{u}_r}_{\text{Centripetal force}} + \underbrace{\Omega \times (\Omega \times \mathbf{r})}_{\text{Coriolis force}} = -\nabla p + \nabla \cdot (\nu + \nu_t) \nabla (\mathbf{u}_r + (\nabla \mathbf{u}_r)^T) \quad (4)$$

The rotation is introduced as two source terms in the momentum equations that account for the Centripetal and Coriolis forces.

2.2.2. Multiple Reference Frame (MRF)

This approach models flow under steady-state conditions using source terms (centripetal and centrifugal forces) into the governing equations to yield desired rotational effects. For wind turbine related problems, two distinct rotational and stationary zones along with periodic conditions along the central axis are required. The following systems of mass and momentum equations are solved in the stationary zone:

$$\nabla \cdot \mathbf{u}_a = 0, \quad (5)$$

$$\nabla \cdot (\mathbf{u}_a \otimes \mathbf{u}_a) = -\nabla p + \nabla \cdot (\nu + \nu_t) \nabla (\mathbf{u}_a + (\nabla \mathbf{u}_a)^T) \quad (6)$$

\mathbf{u}_a represents the absolute velocity as observed from outside the stationary zone, whereas, inside the rotating region, the equations are written in the form of relative velocity \mathbf{u}_r in the following manner:

$$\nabla \cdot \mathbf{u}_r = 0 \quad (7)$$

$$\nabla \cdot (\mathbf{u}_r \otimes \mathbf{u}_r) + 2\Omega \times \mathbf{u}_r + \Omega \times (\Omega \times \mathbf{r}) = -\nabla p + \nabla \cdot (\nu + \nu_t) \nabla (\mathbf{u}_r + (\nabla \mathbf{u}_r)^T) \quad (8)$$

$$\mathbf{u}_a = \mathbf{u}_r + \Omega \times \mathbf{r} \quad (9)$$

In the equation above, p represents the pressure, ν and ν_t show the kinematic and turbulent viscosity. The Ω depicts the angular velocity of the rotating zone. MRF solves for steady-state, and the temporal terms are not accounted for in the governing system of equations.

2.2.3. Sliding Mesh Interface (SMI)

This approach resolves transient flow characteristics around the turbine by utilizing the mesh motion in a sliding manner. The mesh region encompassing the rotor physically rotates with every new time step. This method is proven to be computationally expensive [26,39]; however, it demonstrates realistic estimates against experimental values. The following system of equations is solved.

$$\nabla \cdot \mathbf{u}_a = 0 \quad (10)$$

$$\frac{\partial \mathbf{u}_a}{\partial t} + \nabla \cdot (\mathbf{u}_a \otimes \mathbf{u}_a) = -\nabla p + \nabla \cdot (\nu + \nu_t) \nabla (\mathbf{u}_a + (\nabla \mathbf{u}_a)^T) \quad (11)$$

2.2.4. Turbulence Model

The small-scale turbines in the built environment experience highly turbulent flow in both upstream and downstream directions. It is paramount to resolve spatio-temporal variations of all scales present in the flow field [40]. To resolve small eddies in the RANS approach generated from the energy cascade mechanism from the large eddies, we adopt the $k - \omega$ SST turbulence model as suggested by [41–43]. The details of this particular selection among the range of other models have been previously presented in the studies [27,44] by authors.

The following equations of k and ω [43] have been solved.

$$\frac{\partial k}{\partial t} + \nabla \cdot (\mathbf{u} \otimes k) = \tau_{ij} \nabla u + \nabla \cdot \left[\frac{\nu + \nu_t}{\sigma_k} \right] \nabla (k + (\nabla k)^T) - \omega k, \quad (12)$$

$$\frac{\partial \omega}{\partial t} + \nabla \cdot (\mathbf{u} \otimes \omega) = \frac{\gamma}{\nu_t} \tau_{ij} \nabla u + \nabla \cdot \left[\frac{\nu + \nu_t}{\sigma_\omega} \right] \nabla (\omega + (\nabla \omega)^T) - \omega^2 \beta + 2(1 - F_1) \frac{\sigma_\omega}{\omega} \nabla k \nabla \omega \quad (13)$$

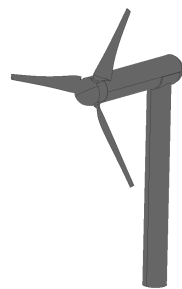
3. Computational Setup

3.1. Geometric Turbine Model

Figure 1 illustrates the 3D CAD model of the small scale HAWT employed in the present work. The turbine blades are built from the 14% NREL S826 airfoil with a twist along the root to tip. NREL S826 airfoil is considered as an effective airfoil shape pertaining to wind turbine designs developed for low Reynolds number flow applications such as in the built environment. The turbine has a diameter (D) of 0.944 m and consists of three blades. The CAD model is modified slightly from the actual experimental model at connections of blades to the nacelle to ease mesh generation.

3.2. Investigated Cases, Mesh, and Boundary Conditions

To explore the effects of various geometric and numerical complexities on small-scale HAWT performance, we categorize the study into five systematic cases. These cases vary depending on a sequential increase in the complexity of the computational model. A new geometric simulation technique is employed to quantify performance parameters keeping fixed operating conditions for each case.









| Parameters | Values |
|-----------------------------------|----------|
| Diameter (D) | 0.944 m |
| Chord length min (c_{min}) | 0.014 m |
| Chord length max (c_{max}) | 0.027 m |
| Blade length (b) | 0.421m |
| Baseline inlet velocity (U_0) | 10.0 m/s |
| Tip speed ratio | 3, 6, 10 |

Figure 1. HAWT-S826: CAD model of the turbine along with description of the geometric parameters.

Table 1 illustrates the domain and boundary conditions employed for each case. Herein, we provide an overview of the case description.

Table 1. HAWT-S826: An overview of geometric approximations employed together with the numerical techniques. Six levels of geometric complexities are considered, i.e., a 2D airfoil (Case-I), 2.5D blade section, 3D full blade (Case-II), 120° blade (Case-III), 360° rotor (Case-IV), and complete turbine structure with a nacelle and tower (Case-V). The first two cases discuss flow around a stationary blade using SRF, while the rest is used to simulate flow around a rotating rotor with MRF and SMI. However, Case-III utilized periodic boundary conditions with SRF for the numerical solution.

| Case ID | Dimension | Rotor | Geometry | Method | Mesh-Size | Geometry |
|----------|-----------|-------|---------------|---------|-------------------|---|
| Case-I | 2D | – | Airfoil | SRF | 8.2×10^4 |  |
| Case-II | 2.5D | – | Blade section | SRF | 9.5×10^4 |  |
| Case-II | 3D | – | Full blade | SRF | 3.5×10^5 |  |
| Case-III | 3D | 120° | Blade | SRF | 9.7×10^5 |  |
| Case-IV | 3D | 360° | Rotor | MRF/SMI | 2.8×10^6 |  |
| Case-V | 3D | 360° | Rotor | MRF/SMI | 4.0×10^6 |  |

Case-I: In this case, 2D computational simulations are conducted for the stationary airfoil to establish validation against experimental data for small-scale HAWT. The baseline computational mesh is shown in Figure 2. Three sets of computational mesh are generated for 2D S826 airfoil with mesh grading ($G_1 = 7.2 \times 10^4$, $G_2 = 8.2 \times 10^4$, $G_3 = 8.9 \times 10^4$) parameters to achieve the mesh independence. The mesh grading of G_2 with 8.2×10^4 cells provide a mesh-independent solution. The $y^+ = \frac{u_* y}{\nu}$ (u_* the friction velocity at the nearest wall, y the distance to the most adjacent wall, and ν the kinematic viscosity) is maintained in the log-law region and varied such that it remains between y^+ of 1. This selection allows the wall functions to calculate the field variables' correct values for the neighboring cells adjacent to the wall. The pressure coefficient profile along the airfoil surface is developed for the α at 0° . The variation of C_d and C_l is quantified as a function of α between 0 and 17° .

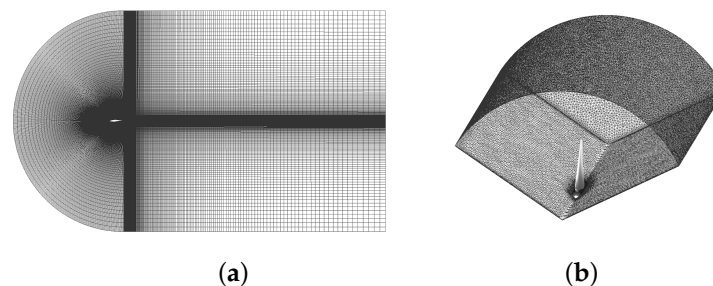


Figure 2. HAWT-S826: Computational mesh for the simulation of flow around the (a) Case-I: S826 airfoil. The computational mesh consists of 8.2×10^4 cells. (b) Case-III: the 120° blade. The hybrid computational mesh consists of 4.8×10^5 cells.

Case-II: This case comprises 2D, 2.5D, 3D simulations conducted for small-scale stationary HAWT. A 2D simulation configuration is similar to the one described in the Case-I. The 2.5D simulation corresponds to the blade section taken along the blade, including tapering of the blade, absent in 2D simulations. In contrast, 3D approximation corresponds to simulations conducted for a full stationary turbine blade. The mesh size was selected after a mesh independence test. The final mesh sizes used for 2D, 2.5D, 3D were 8.2×10^4 cells, 9.5×10^4 cells, 3.5×10^5 cells, respectively.

Case-III: In this case, a 3D analysis of a single rotating blade is conducted with the 120° geometric approximation for small-scale HAWT. The analysis is conducted using MRF and exploiting the axial symmetry of wind turbine rotor blades. The aim is to explore the advantages of fewer degrees of freedom under reduced computational costs to analyze the extent of these simulations to predict wake and aerodynamic coefficients. This configuration is also expected help conduct a parametric analysis of the performance coefficient at various TSR values. The mesh size of 9.7×10^5 cells was achieved after the mesh independence test.

Case-IV: This case represents 3D high fidelity simulations under a 360° rotor; only geometric approximation was used to model rotational effects by SMI and MRF methods. The simulations are conducted for TSR of 6 and 10. The results are demonstrated through variations of obtained wake configuration and aerodynamic coefficients. A hybrid computational mesh is generated for this case. The mesh size of 2.8×10^6 cells was achieved after the mesh independence test.

Case-V: In this case, 3D high fidelity simulations were conducted for full wind turbines, including the nacelle and rotor, using SMI and MRF methods. These simulations provide realistic estimates of the wake, aerodynamic characteristics, and an improved qualitative understanding of the wake through velocity magnitude and vorticity plots. The hybrid computational mesh is generated for this case, as shown in Figure 3. The mesh constitutes structured elements in close proximity to the turbine structure, which transitions to tetrahedral elements in an outward direction. On the one hand, this meshing strategy allows a smooth shift from structured to unstructured mesh elements while reducing the computational cost. A wake block with hexahedral cells is placed in the wake region to

allow accurate wake estimates. The computational domain's overall mesh size consists of nearly 4.0×10^6 cells after the mesh independence test.

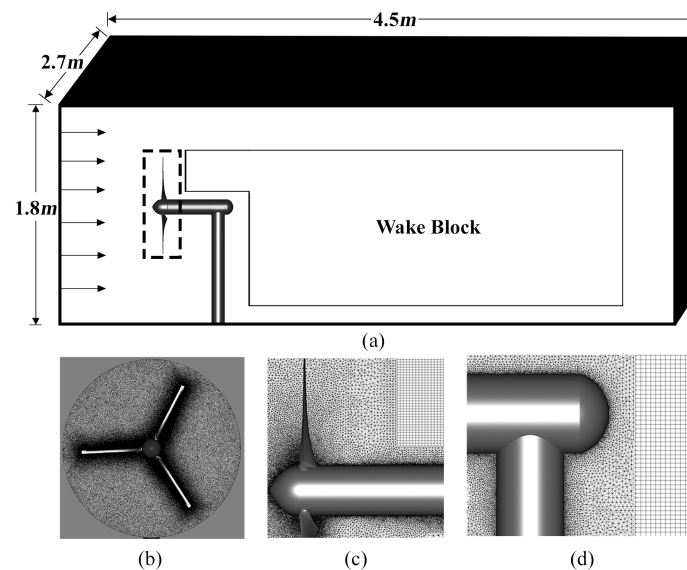


Figure 3. HAWT-S826: The representation of (a) computational domain and (b–d) hybrid computational mesh generated for the full turbine in Case-V. The section view of the turbine blades is also illustrated with the front view and the rotor's snippet. The mesh constitutes structured elements close to the turbine structure which transitions to tetrahedral elements in an outward direction. A wake block with hexahedral cells is placed in the wake region to allow accurate wake estimates. The overall mesh consists of nearly 4.0×10^6 cells.

3.3. Solver Details and Boundary Conditions

The simulations were conducted under an incompressible flow assumption with a fixed fluid density ρ of 1.225 kg/m^3 and the dynamic viscosity μ of $1.82 \times 10^{-5} \text{ kg/m.s}$. The reference flow velocity is set at 10 m/s . The rotational speed is varied such that simulations would be conducted at TSR of 3, 6, 10. The solver is developed in OpenFOAM-6.0 (OF). It uses the Gauss divergence theorem to convert volume integrals into surface integrals over the control volume. The geometric agglomerated algebraic multi-grid (GAMG) is used to solve the discretized equations. The elliptic equation of pressure, momentum, and turbulence equation are solved in a segregated manner using the PIMPLE algorithm (in transient case) or the SIMPLE algorithm (in the steady-state case). PIMPLE is a combination of Pressure Implicit with Splitting of the Operator (PISO) and the Semi-Implicit Method for Pressure-Linked Equations (SIMPLE). The time-dependent variables are solved by the first-order implicit technique to conduct the transient simulations. The Gauss linear corrector solves the diffusion term and the discretization of the convection terms is achieved by utilizing the bounded Gauss upwind scheme. The simulations are run until the convergence criteria is achieved (normalized residuals $\leq 10^{-6}$). In terms of computational resources, the MRF simulation is run on 48 core desktop computers with a 2.6 GHz Intel(R) Xenon(R) processor, and the SMI simulations run on 512 cores with Intel(R) Xenon(R) E5-2670 processor (high-performance supercomputer Vilje).

The boundary conditions applied to the computational domain are depicted in Figure 4 against each selected case. The *inflow* and *outflow* boundary conditions are imposed at the inlet and outlet for each case, respectively. The former uses uniform velocity at the inlet, while the latter uses the zero diffusion flux condition to extrapolate flow values from within the domain close to the outlet boundary. Alternatively, the *no-slip* boundary condition is applied on the blade surface. The axial symmetry is introduced by employing the *periodic* boundary condition in the 120° geometric approximation analysis.

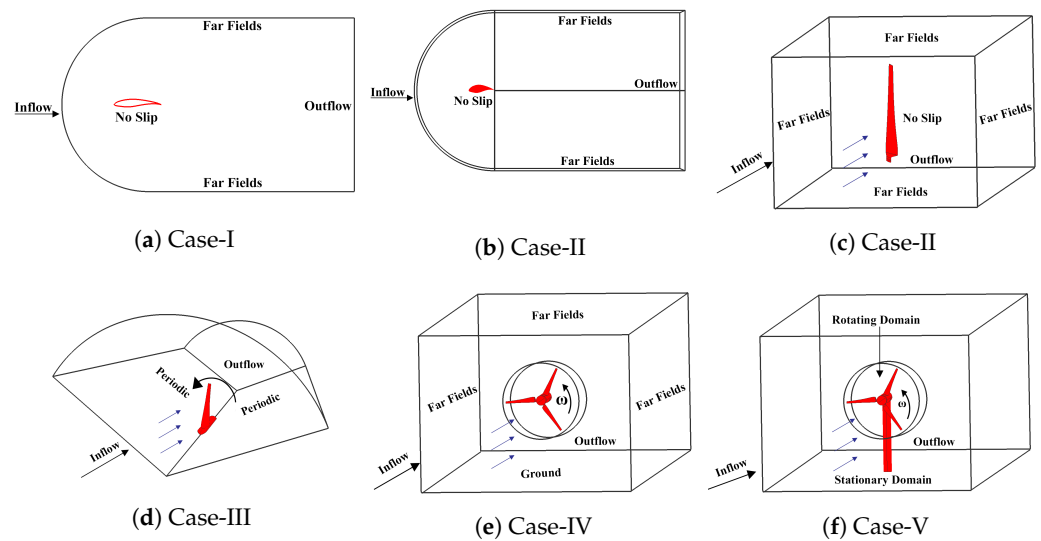


Figure 4. HAWT-S826: Schematics of the geometric approximation with descriptions of the flow directions, flow fields and boundary conditions. Six levels of geometric complexities were considered, i.e., a 2D airfoil (Case-I), 2.5D blade section, 3D full blade (Case-II), 120° blade (Case-III), 360° rotor (Case-IV), and a complete turbine structure with a nacelle and tower (Case-V).

4. Results and Discussion

Now, we present simulation results of geometric and numerical approximation as described in Section 3. Herein, we focus on results with increasing orders of complexity separately against stationary and rotating turbine conditions. In Case-I we first show validation of stationary results against the experimental data for a 2D S826 airfoil. Following the 2D simulations results in Case-II, we compare 2.5D and 3D geometries of an airfoil. After that, we present a detailed comparison of numerical techniques (SMI/MRF) under the geometric approximation of one blade, rotor, and full turbine in Case-III, Case-IV and Case-V, respectively. In the end, we discuss flow structures, wake distribution, and qualitative behavior of wake for different TSRs along with quantification of error.

4.1. Stationary Blade

Wind turbine blades are typically designed to withstand higher stress and moments that originate under dynamic conditions. This modeling strategy usually works well for large megawatt turbine designs, but small kilowatt applications on rooftops would also benefit from stationary blade analysis for long-term successful deployment. Although standstill conditions exist for a short period either due to maintenance purposes, yaw/pitch misalignment, wind gusts, or intermittent wind directions. However, they require careful integration to design calculations, as stationary or semi-stationary states result in a complex flow that generates higher stresses producing additional fatigue loads. Understanding such loads becomes vital from the standpoint of the turbine designer. Herein, we present aerodynamic behavior of the turbine in a 2D/3D configuration to evaluate the extent of numerical predictions in terms of C_d , C_l , C_p .

4.1.1. Case-I: 2D Blade

We conduct a 2D analysis of the S826 airfoil for different values α and validate our results against experimental data of Krogstad et al. [37] for Reynolds number Re_{tip} of 10^5 . Accurate estimation of aerodynamic coefficients (C_l , C_d) is important as the torque generation is dependent on the lift produced by the blade sections. Figure 5a presents the profile of the pressure coefficient for α of 0° along the surface of the airfoil. It can be seen that the airfoil 2D simulation results are generally in good agreement with the experimental data. Note that there are slight differences at the leading edge attributed to the transition from the laminar to the turbulent regime over the blade surface.

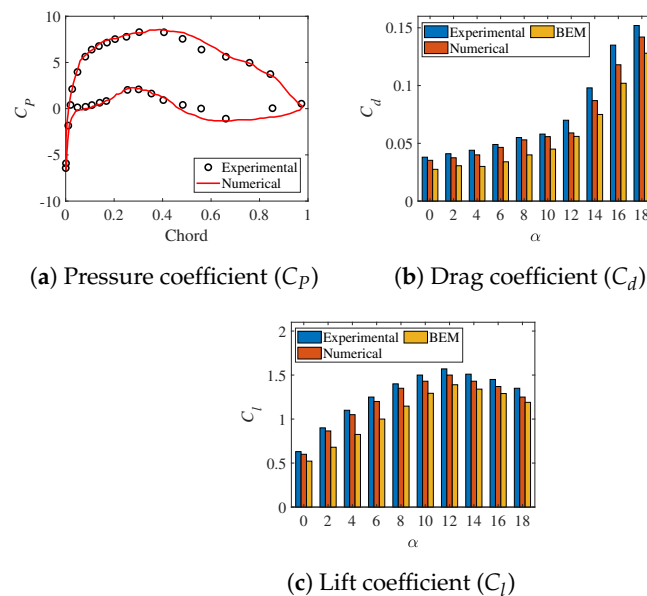


Figure 5. HAWT-S826: Illustration for (a) the pressure coefficient (C_p) versus chord, (b) drag (C_d) and (c) (C_l) lift coefficients versus varying angle of attack (α). Numerical results are plotted against experimental results and BEM (taken from Krogstad et al. [37,38]) at a Reynolds number of 1×10^5 .

Figure 5 presents C_d and C_l as a function of α . The results show accurate estimates of aerodynamic coefficients against experimental and BEM results. The C_d show an increase with an increase in α , whereas C_l first increases and achieves a maximum value corresponding to critical α_{crit} and then starts to decrease again, which is indicative that the airfoil has moved into stall regime. Figure 6 illustrates a flow pattern at range of α . The flow around the blade at α of 0° is symmetrical, which results in a slightly better agreement for lower α values. At higher values of α , the results show relatively less agreement, due to a highly complex flow regime. The critical point identified for the S826 airfoil is α of 12° . A notable rise in the periodic oscillations is observed once α has been increased beyond this point with strong flow separation starting from leading-edge resulting in the evolution of von-Karman vortex street in the wake region. We also notice that BEM under-predicts the aerodynamics coefficients, particularly in the stall region. It can be ascribed to assumptions of strictly 2D flow that have been violated due to stall effects disrupting the assumption of 2D flow that is the basis of the BEM method [38]. Overall, we obtain a close agreement in results from 2D CFD simulations, thereby providing confidence in the accurate selection of solver and boundary conditions.

4.1.2. Case-II: 2D, 2.5D and 3D Blade

In standstill conditions, α between the blade and oncoming flow is determined solely by free wind direction. While the turbine blade design is focused on loads originating under dynamic conditions and relative wind direction, stationary conditions cause the turbine to operate under a narrow operational range [26]. The flow becomes highly complex, and its realistic modeling requires a geometric approximation in the third dimension. We present a comparison of flow behavior for a stationary turbine blade through stepwise characterization in geometric complexity from 2D, 2.5D, and 3D. Four sections along root to tip are considered to determine the extent of flow dimensionality over the blade. Details of each section corresponding to α and chord length are given in Table 2. The quantitative comparison of aerodynamic coefficients is shown in Figure 7. We noticed that a generally good agreement is obtained at blade sections located at the tip compared to those at the hub. For 2D, the error margins for C_l at r of 0.1125 m and 0.42 m are 11.84% and 0.13%, respectively. The same behavior was observed for C_d , which reports error magnitudes in comparison to 3D at r of 0.1125 m and 0.42 m of 25.0% and 0.02%, respectively. This

error was reduced for C_l at 2.5D geometric approximation for r of 0.1125 m to 10.26%, while a marginal increase was observed at r 0.42 m to 0.27%. To illustrate in connection to underlying flow physics, we plot the contours of velocity magnitude in Figure 8. We noticed that three-dimensionality in the flow near the blade hub is the cause of differences in results. The flow remains two-dimensional at the tip; therefore, a better agreement among results from all geometric approximations can be observed. Meanwhile, near the hub center, 2.5D simulations show superior performance than 2D compared to 3D simulations as shown in Figure 9.

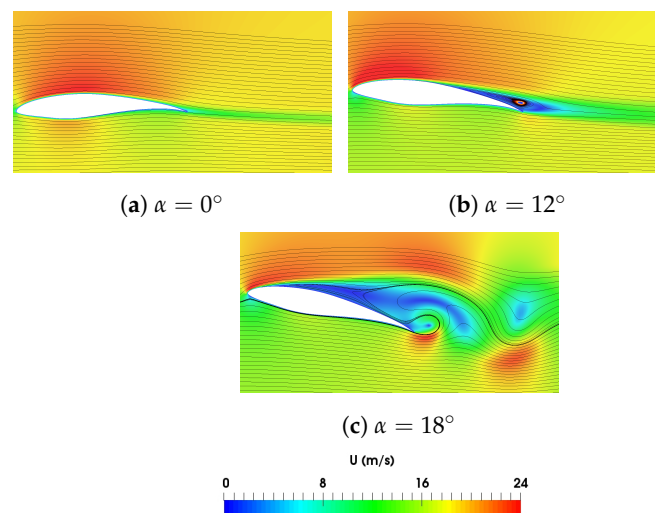


Figure 6. HAWT-S826: Comparison of flow-patterns of the velocity contour (with superimposed streamlines) at α of 0° , 12° and 18° . The streamlines depict the attached, mildly separated and stall regions. At α of 0° , the flow is symmetrical and streamlined; however, at the critical point α of 12° , a notable rise in the periodic oscillations is observed and an increase beyond this point started strong flow separation with the generation of the von-Karman vortex street in the wake region.

Table 2. HAWT-S826: Angle of attack (α) and chord computed over the radial direction along with the error in C_d and C_l for 2D/2.5D geometric approximations, compared to the 3D geometry. The 2D approximation shows a significant error of 25% at the trailing edge, reported in Figure 7, which is reduced as we move down to the leading edge of blade. The 2.5D simulation on the other hand shows improved performance at the leading edge, but the performance drops to 24.42% at the 0.2 m radial direction of the blade. However, it recovers quickly when moving towards the trailing edge.

| Distance from Center (m) | α ($^\circ$) | Chord (m) | Error in C_d (%) | | Error in C_l (%) | |
|--------------------------|-----------------------|-----------|--------------------|-------|--------------------|-------|
| | | | 2D | 2.5D | 2D | 2.5D |
| 0.1125 | 25.262 | 0.073126 | 25.00 | 4.59 | 11.84 | 10.26 |
| 0.2 | 13.067 | 0.051204 | 27.73 | 24.42 | 4.03 | 3.42 |
| 0.3 | 6.565 | 0.036201 | 0.10 | 0.22 | 0.00 | 0.08 |
| 0.42 | 1.097 | 0.02678 | 0.02 | 0.08 | 0.13 | 0.27 |

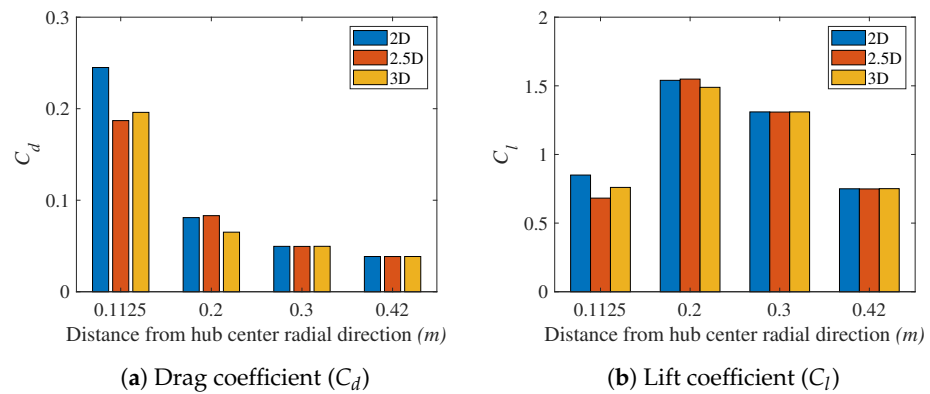


Figure 7. HAWT-S826: Illustration of (a) drag and (b) lift coefficient over the radial direction from the center for 2D, 2.5 and 3D geometric approximations.

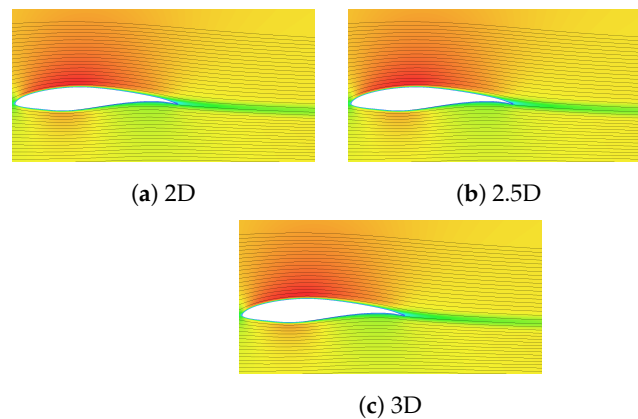


Figure 8. HAWT-S826: Illustration of error for 2D, 2.5D and 3D geometric approximations simulated under similar conditions. The flow patterns indicate strong two-dimensional flow at the outer section of blade. Note: the velocity magnitude is restricted to 0–1 m/s to provide better contrast.

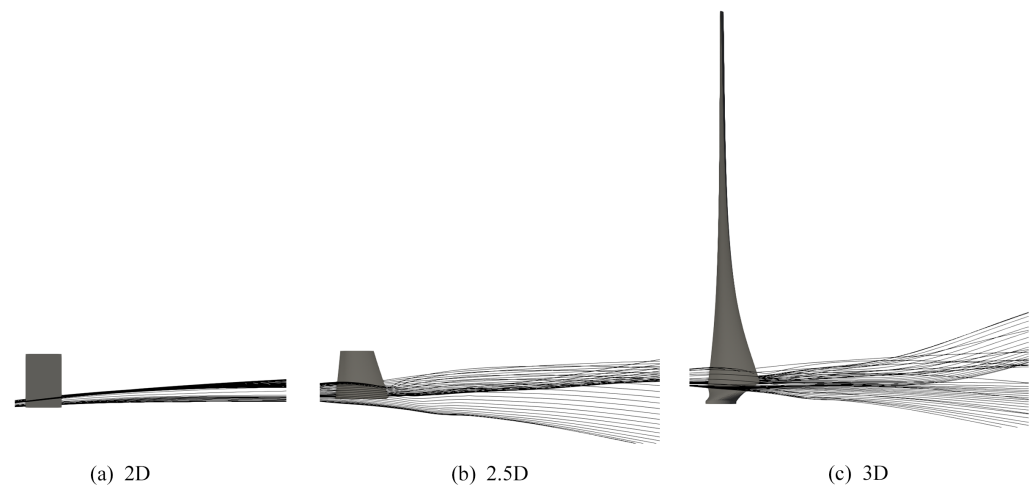


Figure 9. HAWT-S826: Illustration of the top view of flow streamlines for 2D, 2.5D and 3D geometric approximations simulated for the inner section of the turbine blade. The flow patterns indicate strong two-dimensional flow at the inner section.

4.2. Rotating Rotor

To obtain realistic estimates of wake in a downstream direction and an accurate assessment of aerodynamic performances of small-scale HAWT in a built environment, we now perform simulations under the rotational effects. The rotational effects are simulated using quasi-static (MRF) and computationally expensive dynamic (SMI) numerical simulation. The geometric approximation includes the periodic blade, rotor, and the full wind turbine. Herein, we present results to quantify aerodynamic performance (C_p and C_t) and spatial distribution of wake for zero yaw at two positions downstream of the rotor plane, i.e., at x/D of one and x/D of three for Case-III to Case-V. We also provide extensive comparison using qualitative evidence obtained from high fidelity CFD simulations.

4.2.1. Case-III: 120° Blade

We present the results of the single blade modeled under axial symmetry approximation of 120° using SRF. Periodic boundary conditions on the two lateral surfaces account for the rotational effects of the remaining two blades. The average time per iteration of simulations for this case was approximately 2 s. Figure 10 presents the wake profiles behind the turbine at TSR values of 6 and 10. The measurements for x/D of one show good agreement as sharp peaks are captured reasonably well. Note that symmetry in the wake profile appears due to replication of results in the opposite direction for better understanding. The results at x/D of one match the experimental data in the horizontal and vertical downstream direction. A rather good agreement is observed at the blade tip than at the central blade hub. Note that the geometric approximation failed to capture a sharp kink at y/D of 0.2, which is normally anticipated due to the turbine tower's presence.

Following the results at x/D of one, we noticed that at the further downstream location of x/D of three, the wake considerably recovers due to spanwise turbulent diffusion, and plots show a significant reduction in distinct peaks. We also quantify the percentage drop in accuracy in Table 3. Note that, at TSR of six, the error in C_p and C_t is 23.02% and 20.68%, whereas, at TSR of 10, the error is 27.5% and 22.88%, respectively. Both wake profiles and the aerodynamic coefficient show discrepancies in predicted values. The two main reasons for the deviation of results are the absence of other two-blade, nacelle, and support structures and the steady-state assumption while solving the governing system of equations.

Table 3. HAWT-S826: Comparison of cases for the rotating rotor cases, (i.e., Case-III: 120° blade, Case-IV: 120° rotor, and Case-V: complete turbine structure including the nacelle and tower) to quantify the error in the power coefficient (C_p) and thrust coefficient (C_t). The error was calculated against the experimental data at a TSR of 6 and 10.

| | | Case-III | Case-IV | | Case-V | |
|-----------|--------|----------|---------|-------|--------|------|
| | | SRF | MRF | SMI | MRF | SMI |
| C_p (%) | TSR 6 | 23.02 | 11.86 | 8.14 | 5.12 | 3.49 |
| | TSR 10 | 27.5 | 24.5 | 20.5 | 15.5 | 12 |
| C_t (%) | TSR 6 | 20.68 | 13.91 | 11.49 | 8.05 | 4.02 |
| | TSR 10 | 22.88 | 15.42 | 14.41 | 7.29 | 3.39 |

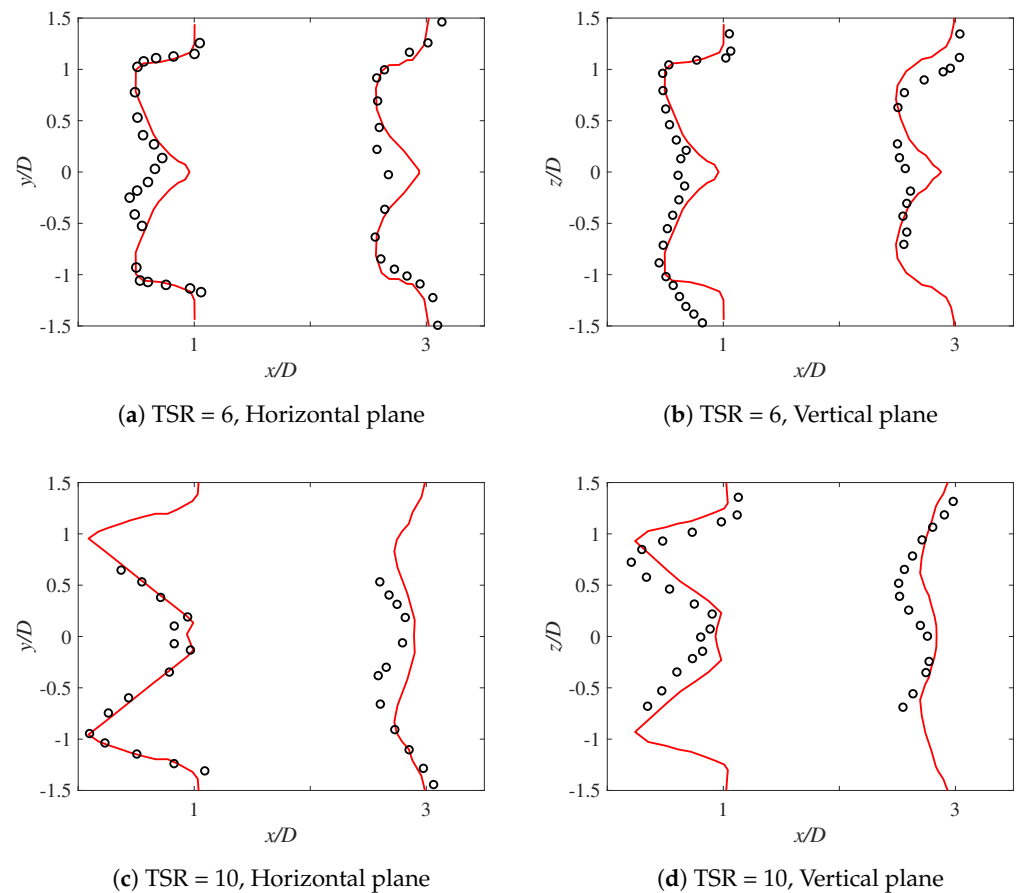


Figure 10. HAWT-S826: Comparison of the velocity deficit using Case-III (a 120° blade with axial symmetry), at successive locations of x/D of 1 and x/D of 3 in the wake region and TSR values of 6 (a,b) and 10 (c,d). Velocity profiles were predicted by MRF (solid lines) with the results of the experiment (circles) taken from [37]. Successive profiles were offset for better clarity.

4.2.2. Case-IV: Rotor Only

We show the results of flow around the turbine rotor using MRF and SMI techniques. The average time per iteration of simulations in Case-IV for MRF and SMI are 4 s and 19 s, respectively. Figure 11 presents the wake profiles plot for TSR 6 and 10. The comparison of wake profiles at x/D of one and TSR of six shows larger oscillation for SMI than for MRF, which arises due to vortices that emanate from the turbine blade and travel in the downstream direction due to transient effects. Note that the recovery rate of the wake is fast in comparison to Case-III. This behavior is ascribed to additional modeling of two blades in MRF, which was absent in Case-III. Similar behavior is observed for TSR of 10; however, the fluctuations in the wake behind the turbine increased considerably compared to that observed in Case-III.

We note that, at TSR of 6, SMI simulations show a better agreement than that for MRF for both axial directions. The wake measurements using MRF at x/D of one and three fail to capture the second peak, which was visible in the experimental results at an approximate distance of y/D of 0.2, whereas SMI predicts this behavior with significantly lower magnitudes. We note similar behavior at TSR of 10 for MRF, but better prediction with the experimental data at x/D of three is obtained. Following MRF results, we notice sharp peaks with large wake expansion in profiles obtained by SMI simulations compared to MRF at x/D of three. In terms of aerodynamic coefficients, C_p and C_t show satisfactory results compared to Case-III. At TSR of six with MRF, the error for C_p and C_t is 11.86% and 13.91%, respectively, while at TSR of 10 a corresponding error of 24.5% and 14.41% can be observed. The SMI simulations, on the other hand, report an error in C_p and C_t of

8.14% and 11.49%, at TSR of 6 and 20.5% and 14.41% at TSR of 10, respectively. Note that SMI indicates a better approximation of results than the MRF; however, the error values predicted at a TSR of 10 are still at the higher end of each method.

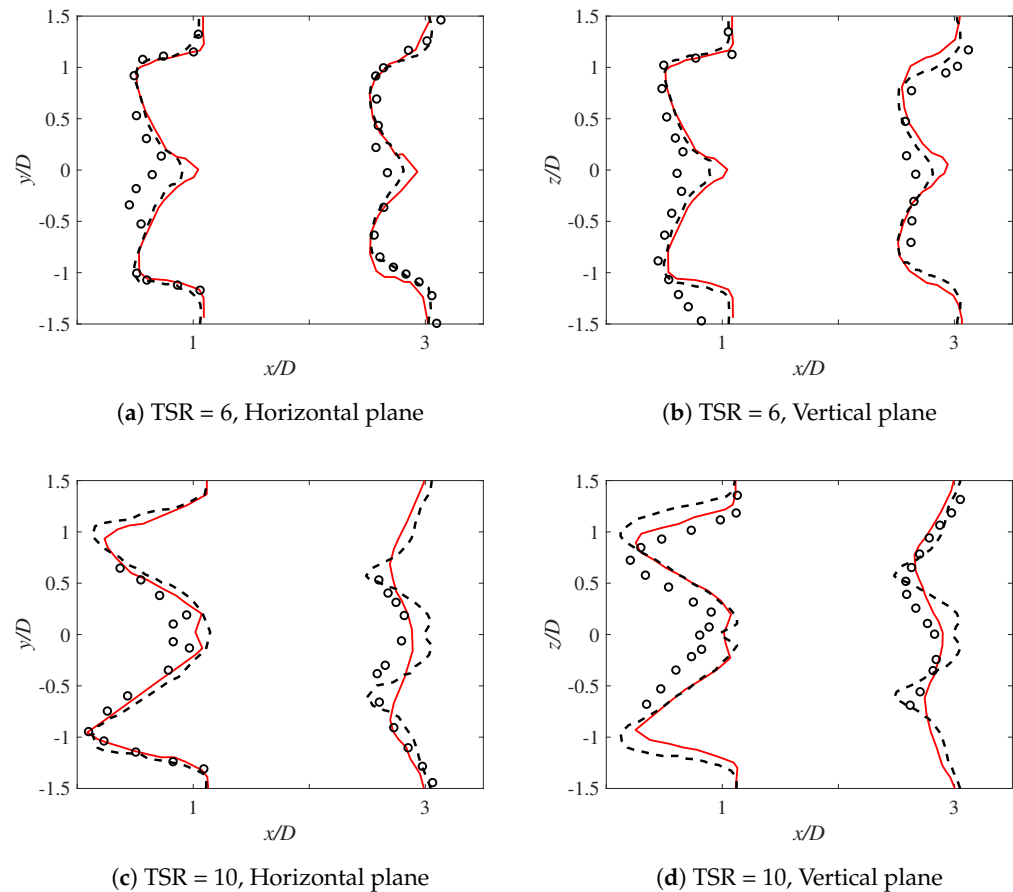


Figure 11. HAWT-S826: Comparison of the velocity deficit using Case-IV (360° rotor), at successive locations of x/D of 1 and x/D of 3 in the wake region and TSR values of 6 (a,b) and 10 (c,d). Velocity profiles were predicted by MRF (solid lines) and SMI (dotted lines) with the results of the experiment (circles) taken from [37]. Successive profiles were offset for better clarity.

To identify the reason for performance prediction under various TSR values qualitatively, we plot the flow field vectors over the domain in Figure 12. We notice that at lower TSR, the turbine is working in the stall mode, due to which three-dimensional effects are dominant over the blade surface. In particular, TSR of 6, the turbine is spinning under design conditions making an optimum angle between the relative wind and blades. It has produced improved lift resulting in the highest production of C_p . Further increase in the TSR to 10 causes the relative velocity to become more in-line with the rotor plane, making flow two-dimensional. It produces larger magnitudes of C_p as compared to the TSR of three. We believe MRF capture such effects particularly well and show close estimates with the measured values. We also notice that MRF results in better prediction than BEM theory with a two-dimensional flow assumption that underpredicts the values at the TSR of three (where in reality the flow has three-dimensional character), unlike the TSR of 10 where an over-prediction is observed with two-dimensional nature of the flow.

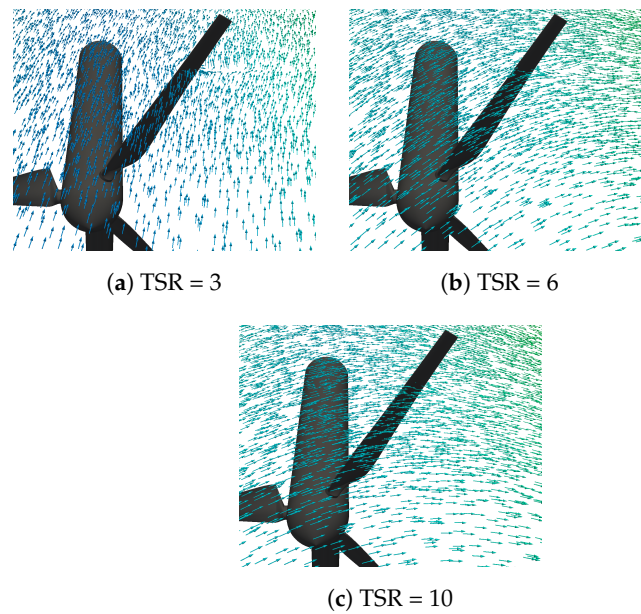


Figure 12. HAWT-S826: Comparison of flow-patterns for Case-IV at TSR values of 3, 6 and 10. At TSR of 3 the turbine operates in stall mode and TSR of 6 corresponds to the design condition, with the flow streamlined in direction to the blade. The flow becomes parallel to the plane of rotation at TSR of 10.

4.2.3. Case-V: Full Turbine

Now, we show high fidelity simulation results for a full turbine with a tower and nacelle. The average time taken for each iteration of simulations in Case-IV for MRF and SMI are approximately 7 s and 30 s, respectively. Figure 13 compares results of wake obtained using both numerical simulation techniques. Note that a good agreement in wake profiles is obtained at TSR of six and x/D of one from both SMI and MRF simulations corresponding to experimental values. In general, at x/D of three, SMI predicts the wake recovery better than the MRF technique for both horizontal and vertical directions. In particular, a sharp kink at y/D of 0.2 along with two other peaks reported in experiments is adequately captured by SMI, which no other geometric approximation manages to reproduce with this much amount of accuracy. While MRF lacks prediction of sudden fluctuations, it manages to reproduce up to a certain extent the kink at y/D of 0.2, which originates due to interaction of blade and tower wake interaction.

Figure 14 show the qualitative behavior of flow around full turbine using each numerical approximation. It is visible that SMI captures sharp features of flow, including tip and hub vortices, while MRF provides an averaged flow field behavior. In terms of prediction of aerodynamic coefficients, Case-V shows a drastic reduction up to three times for error compared to Case-III. We also notice that SMI simulation here outperforms other approximations with an error in C_p and C_t of 3.49% and 4.02% at TSR 6; and 12% and 3.49% at TSR 10, respectively. MRF, on the other hand, shows a marginal difference compared to SMI. For example at TSR of 6 an error of 5.12% for C_p and 8.05% for C_t are reported, whereas at TSR of 10 the error increased to 15.5% and 7.29% for C_p and C_t , respectively.

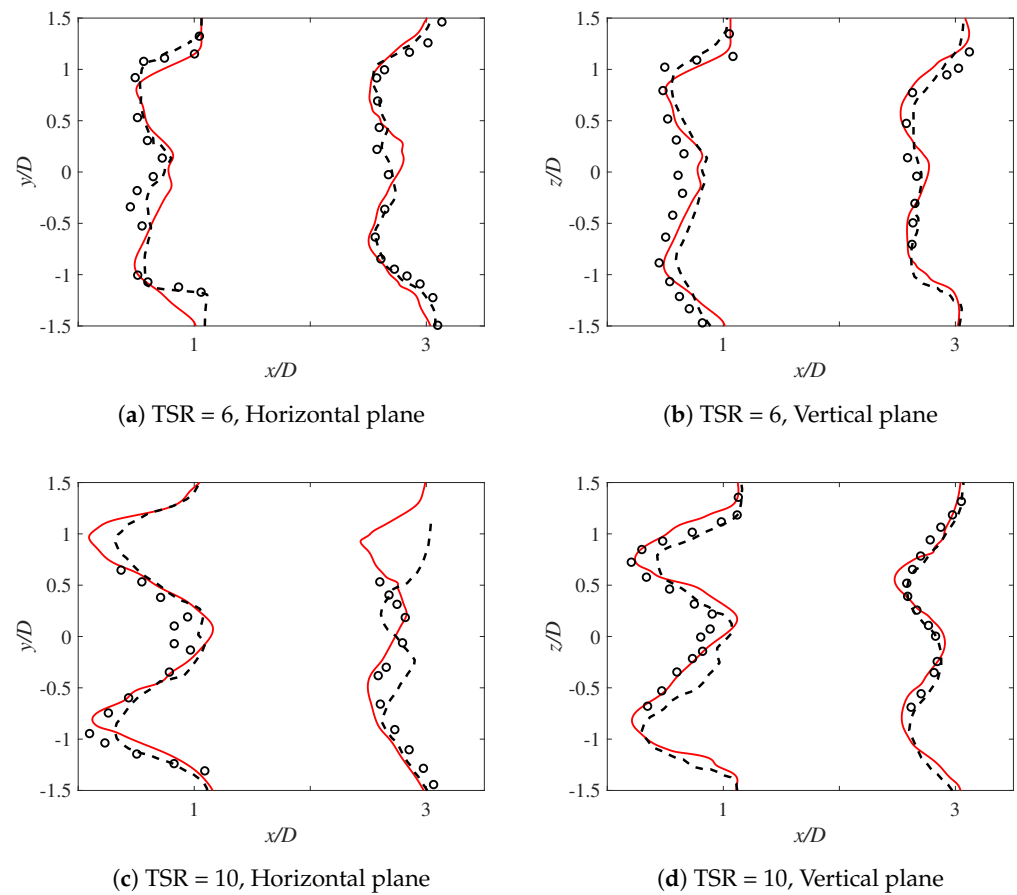


Figure 13. HAWT-S826: Comparison of the velocity deficit using Case-V (complete turbine including the nacelle and tower), at successive locations of x/D of 1 and x/D of 3 in the wake region and TSR values of 6 (a,b) and 10 (c,d). Velocity profiles were predicted by MRF (solid lines) and SMI (dotted lines) with the experimental results (circles) taken from [37]. Successive profiles were offset for better clarity.

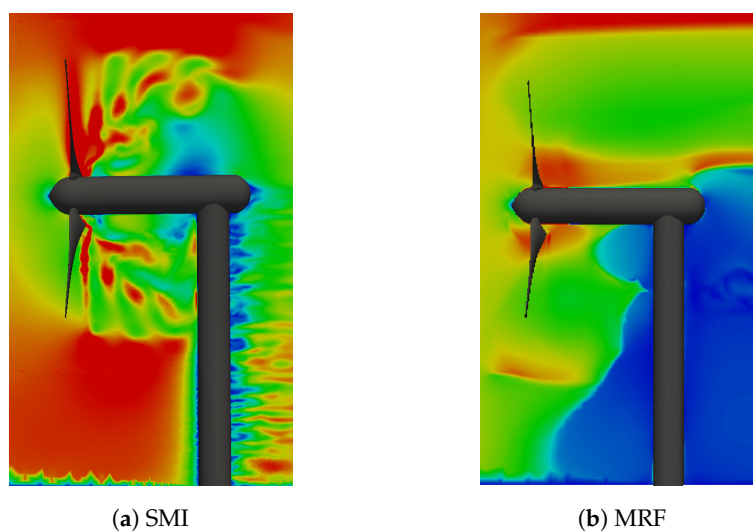


Figure 14. Comparison of flow-pattern for the SMI and MRF simulation techniques on a plane passing through the turbine center. The MRF was shown to provide a good assessment of the large features of the flow field, whereas SMI also accounts for the small features present in the flow field. Note: the velocity magnitude is restricted to 0–1 m/s to provide better contrast.

4.2.4. Qualitative Behavior of Wake versus Tip Speed Ratio

Figure 15 illustrates flow wake dynamics for Case-V at various tip speeds in the downstream direction to examine flow. It describes the contours of vorticity originating from the tower and blade tip. We recognize that the flow is affected by the rotation of the blades and the tower's presence; which was neglected in the previous Case-III and Case-IV.

The wake is characterized by small eddies, whose length and shape depend on the operating TSR. The tower wake is composed of spiral shape vortex structures with tinier scales and representing non-homogenous flow disturbances, whereas the wake formed by the rotor and tower was found to be more homogeneous. The rotor wake is combined with the tower wake, and a vortex pairing can be observed. This pairing is more enhanced in the core behind the tower than the tip of the blade and causes enhanced turbulent mixing and faster recovery of the wake. Regarding the rotor and the tower's wake interaction, we observed the two wakes diffuse together and begin to interact at x/D of one. We also remark that the tip vortices developed until x/D of three; after that, diffusion becomes active and forces the outer wake to combine with the inner vortex core (see Figure 16). A slight shift in the wake towards the leftward side was also seen, which is mainly attributed to the opposite directions of the tower and the rotor wake. Concerning wake width, the simulations predicted an increase in the wake's width in the downstream direction, which is in line with the measured profiles of the wake from SMI and MRF.

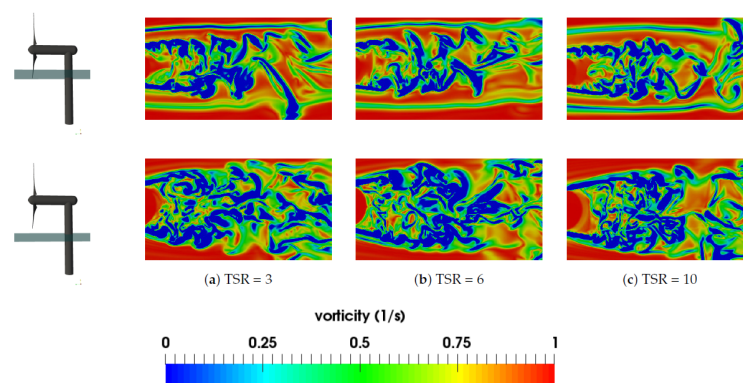


Figure 15. HAWT S826: Vorticity plots exhibiting the formation of coherent structures in two spatial dimensions. Wake is composed of small eddies whose length and shape depends on the operating TSR. The eddies generated by the tower have distinct patterns to those from the combined rotor and tower. Note: the vorticity magnitude is restricted to 0–1 m/s to provide better contrast.

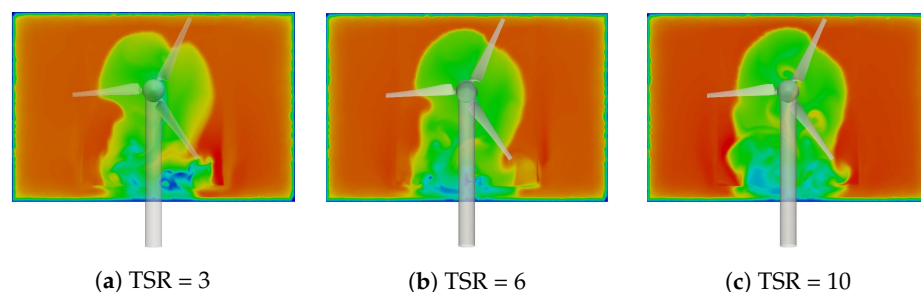


Figure 16. HAWT S826: Velocity magnitude exhibiting the wake distribution at TSR values of 3, 6, 10. Note: the velocity magnitude is restricted to 0–1 m/s to provide better contrast.

5. Conclusions

Aerodynamic analysis of a small-scale Horizontal Axis Wind Turbine (HAWT) was conducted using high fidelity Computational Fluid Dynamic (CFD) simulations to quantify the performance parameters (C_p , C_t , C_l , C_d) and wake profiles. The study was developed based on five selected geometric and numerical approximations of the wind turbine model.

The performance was tested against an incremental level of geometric complexity under the stationary and rotating conditions using the Sliding Mesh Interface (SMI) and Multiple Reference Frame (MRF) simulations. The aerodynamic performance and wake in downstream direction were quantified for each set of geometrical and numerical approximations on a single small-scale HAWT model. The important findings are outlined below.

- In the case of a stationary 2D airfoil (Case-I), the numerical approximations performed better than the blade element momentum (BEM) method, producing close approximations to the experimental results. For the drag coefficient (C_d), the difference from the experiments was minimal until the angle of attack (α) of 12° . The increase beyond this point resulted in the rise of periodic oscillations, which significantly increased the error.
- The 2D simulation performed better than the BEM method at the blade root. However, it is unable to capture complex flow fields near the hub. It was shown that 2.5D captures this effect better with streamlines in three dimensions. The 3D showed superior performance compared to both 2D and 2.5D. We found 25% error for C_d and 11.84% for C_l , at the root tip while the 2.5D model performed relatively better with an error margin of 4.59% and 10.26% for each, respectively. We conclude that flow dynamics can be predicted reasonably well by all three geometric approximations at the blade tip. In contrast, at least a 2.5D geometric approximation must be used for reasonable estimates in the inner section.
- Velocity profiles in the wake region for Case-III show a general good agreement with experiments at x/D of one and three. In contrast, superior predictions were observed for values at the blade tip than the central blade hub. However, Case-III with 120° periodicity failed to capture a sharp kink in experimental behavior at y/D of 0.2 which was anticipated due to the presence of a turbine tower. Case-IV showed a fast recovery rate of the wake due to 360° rotor modeling. However, the measurements from SMI and MRF at x/D of one failed to capture the second peak of the experimental results. The comparison of wake profiles for Case-V showed an overall good agreement with the experiments for both SMI and MRF. While MRF reproduces a partially sharp peak at y/D of 0.2, the SMI captured this and other peaks reasonably well, unlike other geometric approximations.
- In terms of aerodynamic coefficients C_p and C_t , Case-III showed a deteriorated performance with respective errors of 23.02% and 20.68% at TSR of six. The error was significantly increased at TSR of 10 to 27.5% for C_p and 22.88% for C_t . The error was reduced by the inclusion of two more blades in the geometry. Case-IV showed improved performance with error dropping two- to three-fold compared to Case-III. Case-V using SMI; although this was computationally expensive, it showed the most accurate prediction of performance parameters, i.e., an error in C_p and C_t of 3.49% and 4.02% at TSR of six and 12% and 3.49% at TSR of 10, respectively.

An important inference that can be drawn from the present study is that flow investigation using simpler geometric and numerical approximations could be implemented to obtain reasonable results of the flow field around wind turbines. However, one should be aware of limitations in the results from such approximation to drawing plausible conclusions. In the future, we aim to further this study using Large Eddy Simulations (LES) to identify small features of flow in the wake region. Although LES will be computationally expensive, it is expected to help identify enhanced visualization of the wake region downstream of the turbine.

Author Contributions: Conceptualization, M.S.S.; methodology, M.S.S.; software, M.S.S. and M.H.K.; validation, M.S.S. and A.W.B.; resources, M.S.S. and T.A.; data curation, M.S.S. and M.S.; writing—original draft preparation, M.S.S.; writing—review and editing, M.S.S.; visualization, M.S.S. and M.H.K.; supervision, M.S.S. All authors have read and agreed to the published version of the manuscript.

Funding: This research received no external funding.

Institutional Review Board Statement: Not applicable.

Informed Consent Statement: Not applicable.

Data Availability Statement: Not applicable.

Acknowledgments: Part of this work was carried out within NOWITECH (Norwegian Research Centre for Offshore Wind Technology) at the department of mathematical sciences at the Norwegian University of Science and Technology (NTNU). The authors would like to thank Trond Kvamsdal and Adil Rasheed for their valuable suggestions at the start of this research activity.

Conflicts of Interest: The authors declare no conflict of interest.

References

- Behrouzifar, A.; Darbandi, M. An improved actuator disc model for the numerical prediction of the far-wake region of a horizontal axis wind turbine and its performance. *Energy Convers. Manag.* **2019**, *185*, 482–495. [\[CrossRef\]](#)
- Siddiqui, M.S.; Rasheed, A.; Kvamsdal, T. Numerical assessment of RANS turbulence models for the development of data driven Reduced Order Models. *Ocean Eng.* **2020**, *196*, 106799. [\[CrossRef\]](#)
- Siddiqui, M.S.; Rasheed, A.; Kvamsdal, T.; Tabib, M. Quasi-Static & Dynamic Numerical Modeling of Full Scale NREL 5MW Wind Turbine. *Energy Procedia* **2017**, *137*, 460–467.
- Arteaga-López, E.; Ángeles-Camacho, C.; Bañuelos-Ruedas, F. Advanced methodology for feasibility studies on building-mounted wind turbines installation in urban environment: Applying CFD analysis. *Energy* **2019**, *167*, 181–188. [\[CrossRef\]](#)
- Siddiqui, M.S.; Durrani, N.; Akhtar, I. Numerical study to quantify the effects of struts and central hub on the performance of a three dimensional vertical axis wind turbine using sliding mesh. In Proceedings of the ASME 2013 Power Conference, Boston, MA, USA, 29 July–1 August 2013.
- Lu, N.Y.; Basu, S.; Manuel, L. On wind turbine loads during the evening transition period. *Wind Energy* **2019**, *22*, 1288–1309. [\[CrossRef\]](#)
- Nandi, T.N.; Herrig, A.; Brasseur, J.G. Non-steady wind turbine response to daytime atmospheric turbulence. *Philos. Trans. R. Soc. A Math. Phys. Eng. Sci.* **2017**, *375*, 20160103. [\[CrossRef\]](#) [\[PubMed\]](#)
- Churchfield, M.J.; Lee, S.; Michalakes, J.; Moriarty, P.J. A numerical study of the effects of atmospheric and wake turbulence on wind turbine dynamics. *J. Turbul.* **2012**, *N14*. [\[CrossRef\]](#)
- Sharpe, T.; Proven, G. Crossflex: Concept and early development of a true building integrated wind turbine. *Energy Build.* **2010**, *42*, 2365–2375. [\[CrossRef\]](#)
- Wekesa, D.W.; Wang, C.; Wei, Y.; Zhu, W. Experimental and numerical study of turbulence effect on aerodynamic performance of a small-scale vertical axis wind turbine. *J. Wind Eng. Ind. Aerodyn.* **2016**, *157*, 1–14. [\[CrossRef\]](#)
- Bai, C.J.; Wang, W.C. Review of computational and experimental approaches to analysis of aerodynamic performance in horizontal-axis wind turbines (HAWTs). *Renew. Sustain. Energy Rev.* **2016**, *63*, 506–519. [\[CrossRef\]](#)
- Anup, K.; Whale, J.; Urme, T. Urban wind conditions and small wind turbines in the built environment: A review. *Renew. Energy* **2019**, *131*, 268–283.
- Siddiqui, M.S.; Rasheed, A.; Kvamsdal, T.; Tabib, M. Effect of turbulence intensity on the performance of an offshore vertical axis wind turbine. *Energy Procedia* **2015**, *80*, 312–320. [\[CrossRef\]](#)
- Li, L.; Hearst, R.J.; Ferreira, M.A.; Ganapathisubramani, B. The near-field of a lab-scale wind turbine in tailored turbulent shear flows. *Renew. Energy* **2020**, *149*, 735–748. [\[CrossRef\]](#)
- Toja-Silva, F.; Kono, T.; Peralta, C.; Lopez-Garcia, O.; Chen, J. A review of computational fluid dynamics (CFD) simulations of the wind flow around buildings for urban wind energy exploitation. *J. Wind Eng. Ind. Aerodyn.* **2018**, *180*, 66–87. [\[CrossRef\]](#)
- Devinant, P.; Laverne, T.; Hureau, J. Experimental study of wind-turbine airfoil aerodynamics in high turbulence. *J. Wind Eng. Ind. Aerodyn.* **2002**, *90*, 689–707. [\[CrossRef\]](#)
- Ferrari, G.; Federici, D.; Schito, P.; Inzoli, F.; Mereu, R. CFD study of Savonius wind turbine: 3D model validation and parametric analysis. *Renew. Energy* **2017**, *105*, 722–734. [\[CrossRef\]](#)
- Emeksiz, C.; Cetin, T. In case study: Investigation of tower shadow disturbance and wind shear variations effects on energy production, wind speed and power characteristics. *Sustain. Energy Technol. Assess.* **2019**, *35*, 148–159. [\[CrossRef\]](#)
- Abraham, A.; Dasari, T.; Hong, J. Effect of turbine nacelle and tower on the near wake of a utility-scale wind turbine. *J. Wind Eng. Ind. Aerodyn.* **2019**, *193*, 103981. [\[CrossRef\]](#)
- Tangler, J.L. Insight into wind turbine stall and post-stall aerodynamics. *Wind Energy Int. J. Prog. Appl. Wind Power Convers. Technol.* **2004**, *7*, 247–260. [\[CrossRef\]](#)
- Yu, G.; Shen, X.; Zhu, X.; Du, Z. An insight into the separate flow and stall delay for HAWT. *Renew. Energy* **2011**, *36*, 69–76. [\[CrossRef\]](#)
- Troldborg, N.; Sørensen, N.N.; Zahle, F.; Réthoré, P.E. Simulation of a MW rotor equipped with vortex generators using CFD and an actuator shape model. In Proceedings of the 53rd AIAA Aerospace Sciences Meeting, Kissimmee, FL, USA, 5–9 January 2015; p. 1035.

23. Guntur, S.; Sørensen, N.N.; Schreck, S.; Bergami, L. Modeling dynamic stall on wind turbine blades under rotationally augmented flow fields. *Wind Energy* **2016**, *19*, 383–397. [\[CrossRef\]](#)
24. Troldborg, N.; Zahle, F.; Sørensen, N.N. Simulations of wind turbine rotor with vortex generators. *J. Phys. Conf. Ser.* **2016**, *753*, 022057.
25. Tabib, M.; Siddiqui, M.S.; Fonn, E.; Rasheed, A.; Kvamsdal, T. Near wake region of an industrial scale wind turbine: Comparing LES-ALM with LES-SMI simulations using data mining (POD). *J. Phys. Conf. Ser.* **2017**, *854*, 012044.
26. Siddiqui, M.S.; Rasheed, A.; Tabib, M.; Kvamsdal, T. Numerical investigation of modeling frameworks and geometric approximations on NREL 5MW wind turbine. *Renew. Energy* **2019**, *132*, 1058–1075. [\[CrossRef\]](#)
27. Siddiqui, M.S.; Kvamsdal, T.; Rasheed, A. High Fidelity Computational Fluid Dynamics Assessment of Wind Tunnel Turbine Test. *J. Phys. Conf. Ser.* **2019**, *1356*, 012044. [\[CrossRef\]](#)
28. Rocchio, B.; Deluca, S.; Salvetti, M.V.; Zanforlin, S. Development of a BEM-CFD tool for Vertical Axis Wind Turbines based on the Actuator Disk model. *Energy Procedia* **2018**, *148*, 1010–1017. [\[CrossRef\]](#)
29. Guo, Q.; Zhou, L.; Wang, Z. Comparison of BEM-CFD and full rotor geometry simulations for the performance and flow field of a marine current turbine. *Renew. Energy* **2015**, *75*, 640–648. [\[CrossRef\]](#)
30. Tabib, M.; Siddiqui, M.S.; Rasheed, A.; Kvamsdal, T. Industrial scale turbine and associated wake development-comparison of RANS based Actuator Line Vs Sliding Mesh Interface Vs Multiple Reference Frame method. *Energy Procedia* **2017**, *137*, 487–496. [\[CrossRef\]](#)
31. Siddiqui, M.S.; Rasheed, A.; Kvamsdal, T.; Tabib, M. Influence of Tip Speed Ratio on Wake Flow Characteristics Utilizing Fully Resolved CFD Methodology. *J. Phys. Conf. Ser.* **2017**, *854*, 012043.
32. Siddiqui, M.S.; Rasheed, A.; Tabib, M.; Kvamsdal, T. Numerical analysis of NREL 5MW wind turbine: A study towards a better understanding of wake characteristic and torque generation mechanism. *J. Phys. Conf. Ser.* **2016**, *753*, 032059.
33. Tabib, M.; Rasheed, A.; Siddiqui, M.S.; Kvamsdal, T. A full-scale 3D Vs 2.5D Vs 2D analysis of flow pattern and forces for an industrial-scale 5MW NREL reference wind-turbine. *Energy Procedia* **2017**, *137*, 477–486. [\[CrossRef\]](#)
34. Siddiqui, M.S.; Rasheed, A.; Tabib, M.; Kvamsdal, T. Numerical modeling framework for wind turbine analysis & atmospheric boundary layer interaction. In Proceedings of the 35th Wind Energy Symposium, Grapevine, TX, USA, 9–13 January 2017; p. 1162.
35. He, J.; Jin, X.; Xie, S.; Cao, L.; Wang, Y.; Lin, Y.; Wang, N. CFD modeling of varying complexity for aerodynamic analysis of H-vertical axis wind turbines. *Renew. Energy* **2020**, *145*, 2658–2670. [\[CrossRef\]](#)
36. Santoni, C.; Carrasquillo, K.; Arenas-Navarro, I.; Leonardi, S. Effect of tower and nacelle on the flow past a wind turbine. *Wind Energy* **2017**, *20*, 1927–1939. [\[CrossRef\]](#)
37. Krogstad, P.Å.; Eriksen, P.E. “Blind test” calculations of the performance and wake development for a model wind turbine. *Renew. Energy* **2013**, *50*, 325–333. [\[CrossRef\]](#)
38. Krogstad, P.A.; Lund, J. An experimental and numerical study of the performance of a model turbine. *Wind Energy* **2012**, *15*, 443–457. [\[CrossRef\]](#)
39. Cai, X.; Gu, R.; Pan, P.; Zhu, J. Unsteady aerodynamics simulation of a full-scale horizontal axis wind turbine using CFD methodology. *Energy Convers. Manag.* **2016**, *112*, 146–156. [\[CrossRef\]](#)
40. Siddiqui, M.S.; Fonn, E.; Kvamsdal, T.; Rasheed, A. Finite-Volume High-Fidelity Simulation Combined with Finite-Element-Based Reduced-Order Modeling of Incompressible Flow Problems. *Energies* **2019**, *12*, 1271. [\[CrossRef\]](#)
41. Liu, J.; Xiao, Z.; Fu, S. Unsteady transition studies over a pitching airfoil using $ak-\omega-\gamma$ transition model. *AIAA J.* **2018**, *56*, 3776–3781. [\[CrossRef\]](#)
42. Nandi, T.N.; Brasseur, J.; Vijayakumar, G. Prediction and analysis of the nonsteady transitional boundary layer dynamics for flow over an oscillating wind turbine airfoil using the γ - $re\theta$ transition model. In Proceedings of the 34th Wind Energy Symposium, San Diego, CA, USA, 4–8 January 2016; p. 0520.
43. Menter, F. Review of the shear-stress transport turbulence model experience from an industrial perspective. *Int. J. Comput. Fluid Dyn.* **2009**, *23*, 305–316. [\[CrossRef\]](#)
44. Siddiqui, M.S.; Rasheed, A.; Kvamsdal, T. Validation of the numerical simulations of flow around a scaled-down turbine using experimental data from wind tunnel. *Wind Struct. Int. J.* **2019**, *29*, 405–416.